



OPEN ACCESS

EDITED BY

Flavio Cannavo,
National Institute of Geophysics and
Volcanology, Italy

REVIEWED BY

Maged Marghany,
Syah Kuala University, Indonesia
Pietro Milillo,
University of Houston, United States

*CORRESPONDENCE

Chang-Wook Lee,
cwlee@kangwon.ac.kr

SPECIALTY SECTION

This article was submitted to
Environmental Informatics and Remote
Sensing,
a section of the journal
Frontiers in Environmental Science

RECEIVED 13 June 2022

ACCEPTED 27 July 2022

PUBLISHED 26 August 2022

CITATION

Fadhillah MF, Hakim WL, Park S, Kim D,
Park Y-C, Kim C-H and Lee C-W (2022),
Surface deformation simulation for
InSAR detection using a machine
learning approach on the hantangang
river volcanic field: A case study on the
orisan mountain.
Front. Environ. Sci. 10:968120.
doi: 10.3389/fenvs.2022.968120

COPYRIGHT

© 2022 Fadhillah, Hakim, Park, Kim,
Park, Kim and Lee. This is an open-
access article distributed under the
terms of the [Creative Commons
Attribution License \(CC BY\)](https://creativecommons.org/licenses/by/4.0/). The use,
distribution or reproduction in other
forums is permitted, provided the
original author(s) and the copyright
owner(s) are credited and that the
original publication in this journal is
cited, in accordance with accepted
academic practice. No use, distribution
or reproduction is permitted which does
not comply with these terms.

Surface deformation simulation for InSAR detection using a machine learning approach on the hantangang river volcanic field: A case study on the orisan mountain

Muhammad Fulki Fadhillah¹, Wahyu Luqmanul Hakim¹,
Sungjae Park², Daewoo Kim³, Yu-Chul Park⁴,
Chang-Hwan Kim⁵ and Chang-Wook Lee^{1,2*}

¹Division of Science Education, Kangwon National University, Chuncheon-si, Gangwon-do, South Korea, ²Department of Smart Regional Innovation, Kangwon National University, Chuncheon-si, Gangwon-do, South Korea, ³Department of Tourism, Hantangang Geopark, Yeonchun-county, South Korea, ⁴Department of Geophysics, Kangwon National University, Chuncheon-si, Gangwon-do, South Korea, ⁵East Sea Research Institute, Korea Institute of Ocean Science and Technology, Uljin, South Korea

Recent developments in remote sensing research have resulted in a large amount of variability in the data provided by researchers. Synthetic aperture radar (SAR) is a tool used to measure surface deformation and assess changes in the Earth's surface. Here, we consider the usefulness of Interferometric Synthetic Aperture Radar (InSAR) in assessing past volcanic activity as a key to learning the characteristics of the deformation around a volcano. The Hantangang River volcanic field (HRVF) is a geoheritage site in the Korean Peninsula that has interesting geological characteristics. This volcanic field has formed along 110 km of the paleochannel of the Hantangang River. Since the eruptions occurred from 0.15 to 0.51 Ma, the source is limited, which has raised interest in the assessment of volcanic landforms. The recent integration of machine learning and InSAR processing has shown promising results for many purposes, such as classifying, modeling, and detecting surface deformation. To examine the future impact based on information from the past, we utilized a synthetic interferogram with the Okada model and transferred it to a machine learning algorithm. The synthetic interferogram was formed based on Sentinel-1 C-band satellite data to simulate the deformation phases. The orbital errors, the topographical data errors, and the atmospheric effect were also simulated and added to the synthetic interferogram to enrich the learning input. A convolutional neural network (CNN) trained with the unwrapped simulated interferogram data and its performance was evaluated. Our proposed method exhibits the capability to detect volcanic activity's deformation patterns with synthetic interferogram data. The results show that an overall accuracy of more than 80% was achieved using the CNN algorithms on the validation dataset. This study is the first to use machine learning approaches for detecting prehistorical volcanic deformation and demonstrates potential techniques for developing an

approach based on satellite imagery. In addition, this study has introduced the possibility of developing a rapid detection of surface deformation using InSAR data based on a machine learning approach.

KEYWORDS

simulation, InSAR (interferometric synthetic aperture radar), CNN-convolutional neural network, orisan, okada model

Introduction

Volcanic eruptions are destructive events that threaten human life on Earth but can provide benefits such as rich agricultural soils and geological heritage values of volcanic landforms (Siebert et al., 2015). The significant geodiversity of volcanic heritage sites has cultural, scientific, and educational value for local communities (Németh et al., 2017; Casadevall et al., 2019b). These values are recognized by the United Nations Educational, Scientific and Cultural Organization (UNESCO) as a world heritage, and these natural environments are protected by the UNESCO Global Geopark Program (Casadevall et al., 2019a). One of the national geoparks in the Republic of Korea that has been established as a UNESCO Global Geopark is the Hantangang River Geopark (<https://en.unesco.org/global-geoparks/hantangang>). The primary rock in the Hantangang River Geopark consists of stream-eroded basalt, gorges, columnar joints, and river cave geomorphologies formed in the Quaternary Period Cenozoic Era (Lee and Shin, 2019). The Hantangang River Geopark was previously named the Hantangang River Volcanic Field (HRVF) or Hantangang Basalt due to the existence of volcanic basalt adjacent to river valleys (Kil et al., 2019). A series of volcanic eruptions formed the river valley and caused topographical changes in the paleoriver channel that became inundated by basaltic lava flows. The rejuvenated river system eroded the columnar jointed lava, which resulted in the current Hantangang River formation (Woo et al., 2018; Shin et al., 2020).

Orisan Mountain, which is known as the origin of the Hantangang River Volcanic Field (HRVF), erupted in a series of basaltic lava flows approximately 0.15 and 0.51 million years ago, i.e., the eruptions occurred during the late Pleistocene epoch of geologic time (Faul, 1960; Ryu et al., 2011; Kil et al., 2019). Basaltic lava from the Orisan Mountains flowed along a 110 km stretch of the paleoriver channel of the Hantangang River; as this flow length reached over 100 km, it is considered long basaltic lava flow (Keszthelyi and Self, 1998; Kil et al., 2019). This type of lava flow has not occurred in human history or in any geologic records. The rarity of long flows is hypothesized to be related to the lack of effusive basaltic eruptions with volumes greater than 10 km³ (Keszthelyi and Self, 1998). Meanwhile, the general volume characteristics of basaltic volcanic fields fall in the range of 0.1–5 km³ (Valentine and Connor, 2015). Volcanic eruptions are usually associated with seismic activity, in which both events are connected. Seismic activity can reduce the

strength of the magma chamber that leads to an eruption, and significant dike intrusion can induce seismic activity (earthquakes) (Caricchi et al., 2021; Seropian et al., 2021). These events could lead to surface deformation in the volcano topography and its surrounding area (Biggs et al., 2014; Ripepe et al., 2015). The two types of deformation in volcanic eruptions, uplift and subsidence, are caused by the magma inflating the magma chamber and then deflating it due to the volcano's eruption, respectively (Biggs and Pritchard, 2017). A volcanic eruption can be characterized by the deformation caused by seismicity changes that can be recognized by satellite imagery using the InSAR technique (Biggs et al., 2014). Due to seismic activities and volcanic eruptions, the deformation mechanism has been widely studied using Okada modeling (Okada, 1985; Okada and Yamamoto, 1991; Song and Lee, 2019; Fadhillah and Lee, 2021). There was a lack of satellite imagery during the eruption of Orisan Mountain.

Application of machine learning in remote sensing has been developed from the classification for land use or disaster related from optical imagery (Doblas et al., 2020). Besides, classification on amplitude SAR images also has been combined using machine learning approaches for analyzing forest condition or object detections (Lapini et al., 2020; Garg et al., 2021; Li et al., 2022). In terms of application on InSAR data, several machine learning approaches have been employed such as optimization parameter on source deformation using cluster algorithms (Lee and Kim, 2021), volcanic deformation detection (Ghosh et al., 2021; Milillo et al., 2022). Several developments have been made on the InSAR method to increase its effectiveness and reliability in recent years, such as modeling the source of deformation or exploration (Iio and Furuya, 2018; De Novellis et al., 2019). A study conducted by Marghany using fuzzy B-spline in the phase unwrapping process in the DInSAR process (Marghany, 2012a). Deformation analysis development is also carried out using a three-dimensional simulation of coastal deformation (Marghany, 2012b). In order to study deformation, statistical and machine learning approaches are widely applied, such as the use of the Bayesian approach (Bagnardi and Hooper, 2018; Sreejith et al., 2020). The use of machine learning has been used in the analysis of the source of deformation with the method of artificial neural network (Lee and Oh, 2018) and the use of principal component analysis to optimize the parameters of the source of deformation (Remy et al., 2014). In the semi-automated process of deformation detection using SAR data on Volcán De Colima in Mexico and Mt. Thorbjorn in Iceland using the machine

learning algorithm. This detection focuses on detecting volcanic deformation signals on interferogram patterns using synthetic data based on mogi model source deformation (Ghosh et al., 2021). Therefore, several study has been carried out to analyze deformation using multi resource and combination of algorithm in geological and anthropological events. Based on the description of the previous research found several obstacles that affect the level of reliability of the method. Some of these things include human manual intervention in determining the operational parameters used in model training, the imbalance of training input data used causes risk in determining model results (Iio and Furuya, 2018; Anantrasirichai et al., 2019; Yang et al., 2020). Besides, network structure of algorithms should be reliable to get better results with many combinations (Krizhevsky et al., 2017). In addition to the operational parameters based on machine learning algorithms, the quality of the input data also affects the output results. The deformation of Mount Baekdu has been modeled using InSAR simulation data with various VEI indices limited to a single-interferogram (Achmad et al., 2020). One of the limitations is the effect of atmospheric error and decorrelation which commonly appears in the interferogram. Atmospheric and topographic corrections are needed to improve the quality of the interferogram to maximize the deformation pattern detection process using machine learning algorithms. In addition, the application in ancient volcano areas is still minimal in literature, where comparative field data is limited.

Therefore, in this research, we try to apply deformation detection to the ancient mountain Orisan Mountain on the Korean Peninsula. The InSAR deformation detection studies on ancient mountains are still rarely carried out so that the existing references focus on the use of geological and other field data. The approach to the study of ancient volcanoes can provide new insights in the application of remote sensing in understanding these geological events, especially on Mount Orisan. In this research, we use SAR data from the Sentinel-1 satellite as the basis for synthesizing interferograms in Orisan Mountain. As for overcoming the data imbalance, we use data augmentation techniques in the training process using the interferogram algorithm. This process is a simple process compared to other steps carried out without reducing the focus on the InSAR-based deformation review. As a result, the aim of this study is to estimate the source of surface deformation of the Orisan Mountain eruption through Okada modeling calculations. The results of this study can be used as a preliminary study to determine the mechanism of volcanic activity that occurred in the Orisan Mountain.

In this research, we aimed to exploit the ability of a CNN deep learning algorithm to detect deformation signals from interferogram data. Synthetic interferogram data were used to overcome the lack of availability and imbalance of training datasets. Synthetic interferograms were composed of the deformation signal and some of the commonly encountered errors in InSAR process that have been modeled. Deformation

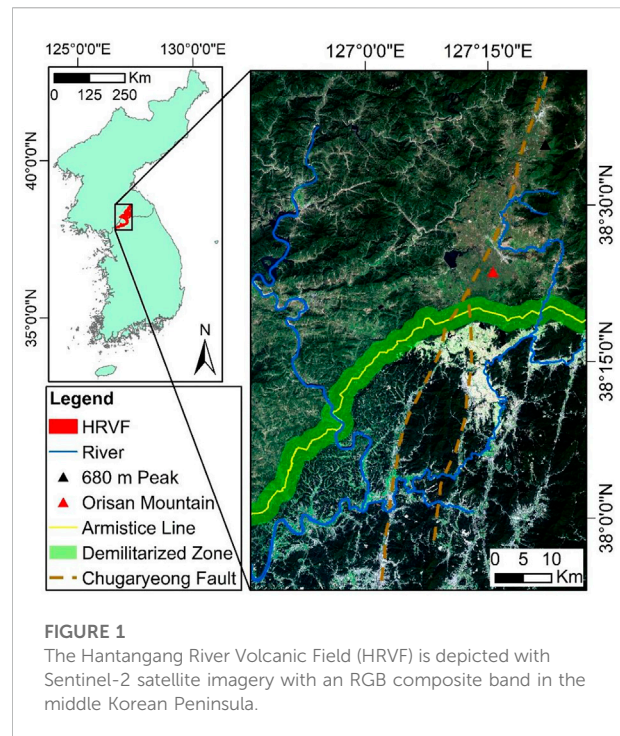


FIGURE 1
The Hantangang River Volcanic Field (HRVF) is depicted with Sentinel-2 satellite imagery with an RGB composite band in the middle Korean Peninsula.

modeling with the Okada method, which is quite simple and is widely used in volcanic deformation modeling, was used as a source of synthesized deformation signals. For error modeling, we used topographic error modeling with isotropic two-dimensional fractals, orbital disturbances using the polynomial method, and simulations of atmospheric disturbances based on topographical modeling. In the interferogram classification process with the CNN model, we used an efficient transfer learning strategy with a pretrained network architecture, namely, ResNet-18, ResNet-50, and AlexNet. To the best of our knowledge, the usefulness of the interferogram classification method with a CNN deep learning algorithm has never been applied to ancient volcanoes, which have limited data availability and are therefore a challenge in this research. Nevertheless, the classification performance test on volcanoes was carried out by testing the classification accuracy and presenting an analysis of deep learning detection. In addition, the use of the CNN classification method was not only aimed at increasing knowledge about volcanic activity but was also aimed at inspiring an initial study of the development of ancient volcanic deformation detection. Additionally, this research can inspire the development of rapid detection of surface deformation from InSAR data based on deep learning algorithms in the future.

Study area

The Hantangang River Volcanic Field (HRVF) is known to have been formed by lava sources from Orisan Mountain, which

is located at 38°23'27" N, 127°16'5" E, in the Democratic People's Republic of Korea (North Korea), with a peak height of 444 m above sea level (Woo et al., 2018; Kil et al., 2019). This volcanic field consists of basaltic lava flow that spread along the middle of the Korean Peninsula, as shown in Figure 1. The Hantangang River is the primary water resource that contributes to various uses in local communities (Cho et al., 2020). Based on topographical analyses and aerial photographs of the Hantangang River Volcanic Field (HRVF), it has been suggested that this field originated from Orisan Mountain, which erupted with a fissure eruption along the Chugaryeong fault system (Kil et al., 2019). Recorded fault events occurred along with volcanic eruptions in the Chugaryeong fault system during the Quaternary period; this fault system is located along the study area (Shin et al., 2020). The geological conditions around the study area most consist of Precambrian and Paleozoic metamorphic rocks, Mesozoic Jurassic and Cretaceous granites, Mesozoic Cretaceous volcanic rocks, and Quaternary Hantangang River basalts (Kil et al., 2019). Fluvial sediments overlay the unique geological conditions of the Hantangang basalt with pillow lava features (Woo et al., 2018).

Materials and methods

The deformation simulation of the late Pleistocene eruption of Orisan Mountain that formed the Hantangang River basalt was produced by implementing a synthetic deformation interferogram. The synthesized data and deformation models were carried out in various studies (Lee et al., 2012; Achmad et al., 2020). Several studies have provided the deformation model such as analyze the source of deformation and the magma chamber were determined by using the Mogi model (Mogi, 1958) and simulated the mechanism of the deformation source from the eruption of Mount Etna and earthquakes using the Okada model (Okada, 1985; Okada and Yamamoto, 1991). In addition, the synthesis data were used as training data in the automatic process of detecting volcanic eruptions. Synthetic data generated from the modeling process can mimic what happened during the eruption.

The synthetic deformation map takes into account the LOS deformation based on the strike-slip and dip-slip faults, source depth, strike angle, and slope angle. In addition, we considered geometric aspects such as length and width based on the Okada model. After the deformation map was generated, we included various errors in the deformation map to obtain a synthesized interferogram. Atmospheric disturbance was added to reflect the delay due to changes in the atmosphere during data acquisition. In addition, topographical errors and orbital errors were used to interfere with the deformation model and were generated using the Okada model.

Synthesis of the synthetic aperture radar interferogram process

To create InSAR simulation data in this study, we used the single look complex (SLC) data from the Sentinel-1 satellite with a wavelength of 5.6 cm. Using the two SLC images from this satellite, we obtained an image of the interferogram and the unwrapped phase as input for the deformation synthesis process. Before the process was carried out, the SLC data obtained were coregistered with subpixel level accuracy to reduce geometric errors and increase spectral diversity in the interferogram process and we used 8×2 multilook factor for range and azimuth directions (Li and Bethel, 2008). For the topographic phase reference, we used the digital elevation model data from the SRTM with a resolution of 1 arc-second (30 m) (Farr et al., 2007). The result from the interferogram process was used as input for the synthetic deformation interferogram simulation. In this study we simulated an interferogram based on the Sentinel-1 SAR satellite with a wavelength of ~5.4 cm using the full resolution of the phase array in the range and azimuth described by (Amelung et al., 1999). In the interferogram there are various phases that compose an interferogram which can be described as follows.

$$\Delta\varphi = \varphi_{topo} + \varphi_{atmo} + \varphi_{deform} + \varphi_{noise} + \varphi_{err}$$

The phase includes the effect of topography φ_{topo} , atmospheric conditions on data acquisition φ_{atmo} and also phase noise which consists of various kinds of errors, one of which is orbital error φ_{err} . However, of course, the surface deformation phase that is the target of the research is included in the interferometry phase. Therefore, in this research, we conducted the formation of an interferogram simulation by compiling a surface deformation signal using the Okada Model and the formation of a more detailed error simulation will be explained in the method section below. The Okada model is one of the inverse modelling methods used to determine the deformation source based on rectangular slip faults and is widely used for volcanoes and earthquakes (Okada, 1985; Okada and Yamamoto, 1991; Fadhillah and Lee, 2021). In the modeling process, geometric data such as length, width, and depth are considered to obtain an idea of how the deformation may have occurred. The additional geometric parameters that need to be utilized are the strike angle and the strike-slip fault. With this information, the possibility of deformation of volcanoes can be obtained, mainly those with dike intrusion in their deformation (Albino et al., 2019; Bonforte et al., 2019). The parameter assumptions to generate the synthetic deformation interferogram were based on data from seismic activity on the Chugaryeong fault and previous volcanic eruptions (Shin et al., 2020). The changes in surface deformation could be further estimated by referring to the volcanic eruption ejecta volume based on the volcanic explosion index (VEI) (Newhall and Self, 1982). We

categorized the explosivity of the effusive eruption in the Orisan Mountain as ranging between 1-3 VEI.

When synthesizing the deformation map data with the Okada model, there are two steps after determining the operational parameters. The first step is to use the Levenberg–Marquardt algorithm to obtain the slip mechanism and fault geometry in a non-linear optimization process. The Levenberg–Marquardt algorithm is a general confidence area method for non-linear calculations (Moré, 1978). This algorithm can be considered as a combination of the Gauss-Newton method and the steepest derivation method in the calculation process (Coleman and Li, 1994). This can be described by the behavior of the damping parameter which works like a steep drop method when the point is far from the correct solution. However, the conditions will change and work like the Gauss-Newton method when this point is close to the correct solution. In its application the algorithm is generally used in the case of infinite non-linear optimization, although this algorithm can be developed for constrained problems. Some of the region of belief methods used include the trust-region reflective and the Dogleg method (Lee and Kim, 2021). The second step is the iteration process using the Monte-Carlo restart method to obtain a linear inversion and avoid falling into local minima during the iteration process (Achmad et al., 2020). In addition, we can use a Monte-Carlo restart which generates many initial starting points and then solves the non-linear least squares problem for each starting point as well as obtaining results from multiple starting points helps to find the global minimum. After defining the boundaries of operational parameter, the algorithm performs a Monte-Carlo restart for the wide initial search space described in the operational parameters. Since the Strike, Dip and opening parameters represent angles, the lower and upper bounds defined in the range are physically available. The geometry parameter of the fault which is described in units of length is defined to be able to describe the maximum movement that may occur in the study area. Then, restarting the Monte-Carlo is done to get the combination of parameter pairs for the next deformation simulation. In order to expedite the restart process, it is carried out with five thousand iterations. And in order to calculate the loose termination tolerance of the non-linear method we used a random subsample of 20% of the measured deformation data to be extracted and analyzed. In solving the non-linear least squares problem, we aim to minimize the objective function $\|G(m)_{smp} - d_{smp}\|_2$ to take the parameter that best fits the minimum residual. As a result, the corresponding m_i^* and RMSE optimization results are calculated in each iteration. The synthetic deformation map image that is projected on a three-dimensional surface changes based on the Line-of-Sight satellite.

After obtaining the deformation model of the Okada process it will be called simulated deformation phase (φ_{sim_deform}), we also simulated the phase errors that often appear in InSAR such as topographic errors (φ_{topo_err}), atmospheric effect (φ_{atmo_err}), and orbital errors phase (φ_{orbit_err}). Those simulated error phase will be summarized to become simulated error phase (φ_{sim_err})

$$\varphi_{topo_err} + \varphi_{atmo_err} + \varphi_{orbit_err} = \varphi_{sim_err}$$

The error phase is simulated with calculations which are described in more detail in the (3.2 Simulated Error Generation) section. Then to integrate the fault simulation phase with the deformation simulation phase we add up the phases into an interferogram simulation phase. We show the flowchart of the simulated interferogram process in Figures 2A–E.

$$\varphi_{sim_deform} + \varphi_{sim_err} = \Delta\varphi_{sim_insar}$$

Simulated error generation

In this synthesis process, we added the effects of atmospheric changes that may occur during data acquisition at different times. Atmospheric disturbance is one of the most common disturbances in interferograms and dominates the signal-to-noise ratio and decorrelation noises. In general, atmospheric disturbances are correlated with altitude and often occur in mountainous areas (Remy et al., 2015). Differences in water vapor conditions and pressure affect the phase delay in data acquisition. This atmospheric error can be formulated as follows (Biggs et al., 2007; Lee et al., 2012).

$$atmo(x, r) = a_0 + a_1 H_0(x, r)$$

where a_0 is the phase constant, a_1 is the slope phase, and H_0 is the area's height at the x and r coordinates.

In addition to atmospheric disturbances, we also added tropospheric disturbances associated with errors in topography and baseline effects. The topographic error is caused by disturbances in the DEM value used in the interferogram formation process. One of the methods used in the topographic simulation is the isotropic two-dimensional fractal surface, which can be represented in the following formula (Masterlark, 2007).

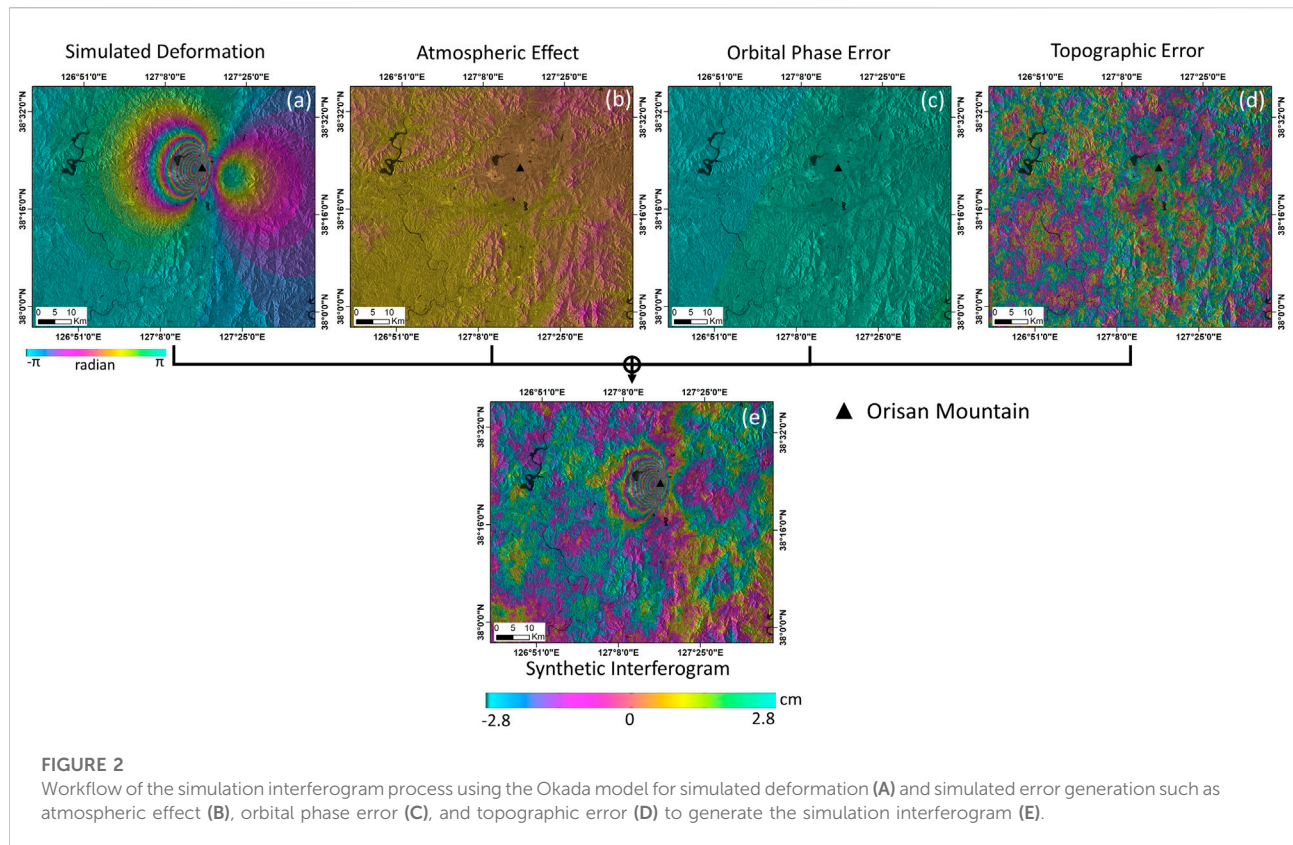
$$\Delta\phi_{topo}(x, r) = \frac{4\pi B_{perp}}{\lambda r \sin\theta} \Delta z$$

where $topo$ is the topographic error phase that exists in the interferogram with the baseline perpendicular to the range is obtained with azimuth at the r and x coordinates, and λ is the satellite wavelength SAR. Finally, we have the addition of the orbital error that affects the SAR data acquisition process using the first-order polynomial method (Lee et al., 2012). The distortion limit caused by the orbit is limited to approximately 4 cm in each image.

$$\Delta\varphi_{orbit}(x, r) = ax + br + c$$

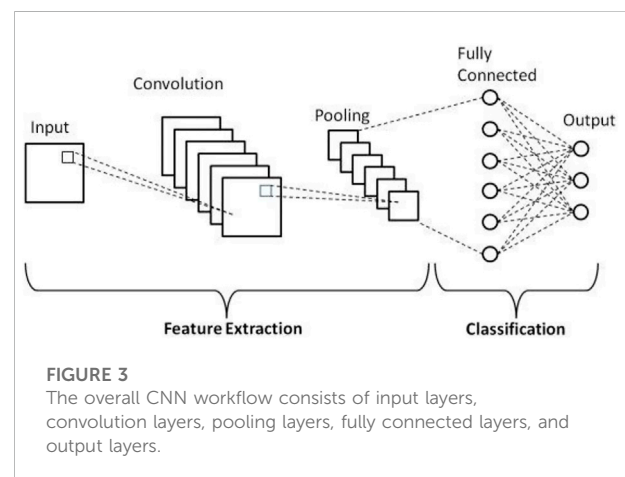
Convolutional neural network

The application of machine learning has become a popular approach in the analysis of image data such as those obtained

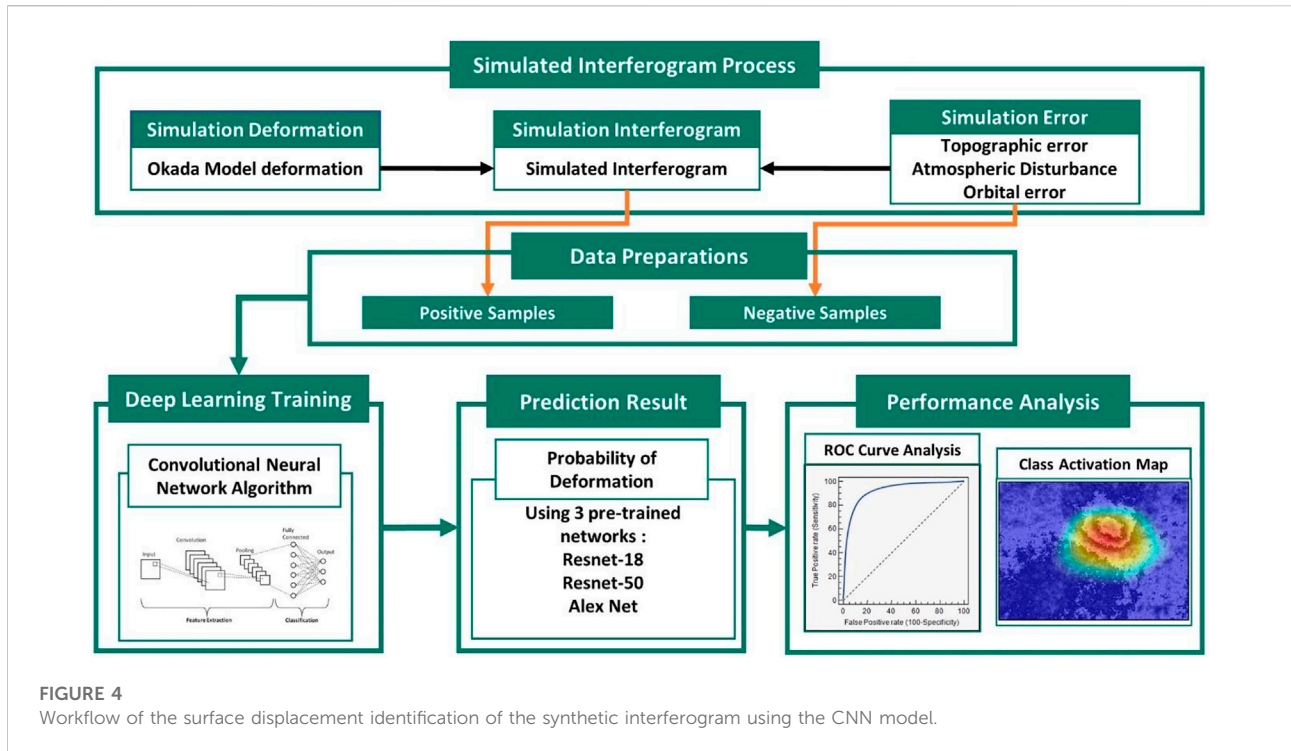


from remote sensing. ML offers data analysis, and patterns in the input image can be separated into classes that have been studied or predefined. One of the popular and well-known ML models is the convolutional neural network (CNN), which relies on the hierarchical feature learning method in the database, and the advantages of feature extraction on the data make CNN more adaptive without user intervention. From generating disaster hazard maps to predicting deformation analysis, the CNN model has been widely used in the geospatial field. By using the CNN and a metaheuristic algorithm, the reliability of generating landslide susceptibility mapping in South Korea was demonstrated (Hakim et al., 2022a). In addition, CNNs were used to build an automated system for surface deformation analysis using SAR data from volcanoes (Anantrasirichai et al., 2019; Valade et al., 2019).

In general, CNN, which is a learning model that can extract features from data, is composed of five main layers, namely, 1) a convolution layer, 2) a normalization layer, 3) an activation layer, 4) a pooling layer, and 5) a linear layer, as shown in Figure 3 (Bregman and Barnhart, 2021). The convolutional layer is an important element in CNN and is combined with filters to analyze the input image. The size of this filter is generally small (5x5 pixels) and is used in the training process to learn and identify more specific features in the input data. In the



interferogram application, this filter is used to identify the frequency fringes, fringe shapes, or areas of surface deformation to study the deformation patterns in the input data. Then, these filters are applied to the input and output images and they relate to how well the features identified in each filter are represented in the input data (Panahi et al., 2020; Hakim et al., 2022c).



After being processed in the convolutional layer, the output data is standardized during the training process in the normalization layer. The aim of normalization is to reduce the amount of training required and increase the learning efficiency in each network (Sameen et al., 2020). The output of the normalization process is processed in the activation layer, which is where the data are input for the next process. The pooling layer aims to reduce the sample output from the convolutional layer. The pooling layer allows the CNN to better identify information on features that have changed, such as shifts, rotations, or chunks in the input data. In terms of the interferogram process, this is useful for identifying different deformation magnitudes or fault orientations in objects (Long et al., 2015). The last layer is the linear layer, whose task is to translate spatial information in the CNN model into activation, which is a probability for a certain network class. In its application, the linear layer takes the final pooling layer and translates it as a possible input image containing only noise or containing surface deformation mixed with noise. In the development of a CNN model, different numbers of these layers can be combined in a variety of ways. The various CNN network structures can provide their own advantages according to the characteristics of the network, and some well-known network structures include AlexNet and ResNet (He et al., 2016; Krizhevsky et al., 2017; Zhao et al., 2021). The whole workflow of this research is shown in Figure 4 and consists of the simulation interferogram process and the learning process for detecting the surface deformation pattern. In the

CNN training process, we used pre-prepared interferogram simulation data. In this process, the CNN method will study the fringe pattern associated with the case of surface deformation. In addition, an error phase related to topographical and atmospheric errors was also prepared to anticipate learning errors related to the deformation fringe pattern. The error simulation phase which consists of simulating topographical errors, atmospheric disturbances and orbital errors is categorized into negative samples in the dataset. Each sample will then be randomly selected in the training process to study the fringe pattern. In addition, some of the datasets, namely the testing dataset, were also used to validate the training process in order to obtain an analysis of the model's performance. In this training process, we use three pre-trained networks that already have reliability in image classification. The use of this structure aims to minimize the process of trial and error in the combination of structures and try to apply it to the introduction of interferogram data.

Results

synthesized interferogram results

The deformation phase was simulated using the Okada method. The adjustment of the operational parameters of the simulation was based on existing literature on this topic. In addition, the calculation of the phase error that often appears in

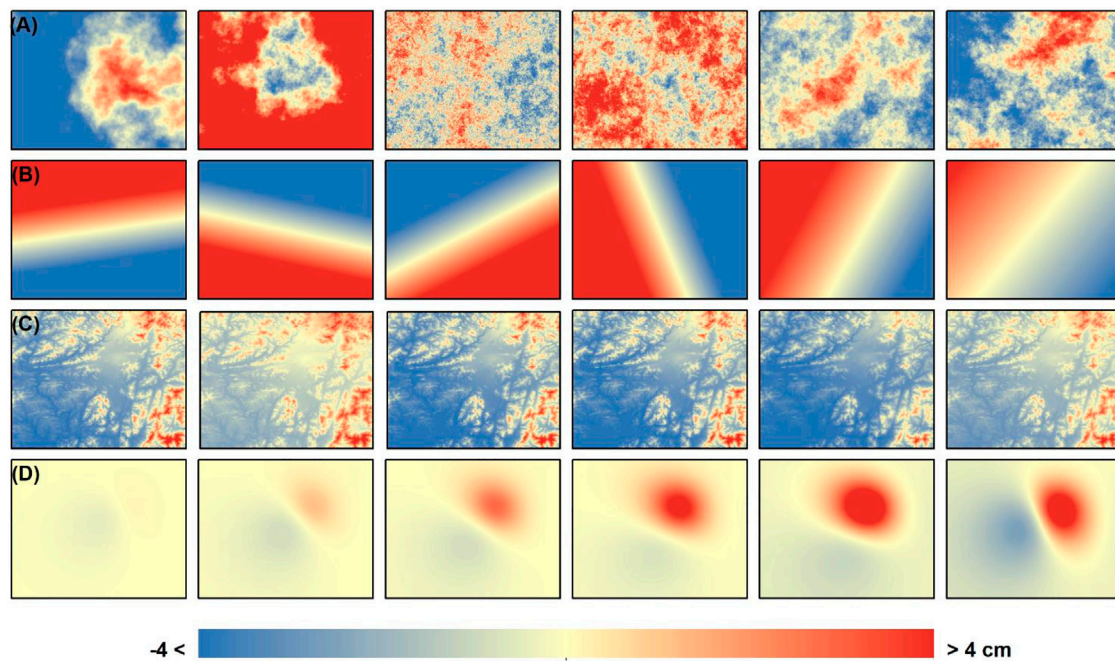


FIGURE 5

Examples of the synthesized image results of (A) topographic errors, (B) orbital errors, (C) atmospheric disturbance, and (D) surface deformation model using the Okada model.

the interferogram was added to the deformation model. Then, the simulated deformation signal and error phase were generated and are shown in Figure 5. These images were also used for the training process of the CNN. Data were separated into two datasets: 2-class datasets and 4-class datasets. The 2-class datasets consisted of labelled and non-labelled deformations for the training process. The non-labelled deformation was a form of the simulated error phase, including the topography error, atmospheric disturbance, and orbital error. Meanwhile, the labelled deformation was composed of the synthetic interferogram image generated by the deformation model and the simulated error. The 4-class datasets consisted of the labelled deformation and the separate simulated errors (i.e., the topography error, atmospheric disturbance, and orbital error) for the training process.

The results of the interferogram synthesis can be seen in Figure 6 and include various available operational parameters. Here, the synthesis of the interferogram was simulated with deformation changes based on the possible VEI levels, namely, the 1–3 scale. In addition, the change in deformation was based on the probability level of lava flow, which is the basis for this study, where lava can flow as far as 100 km to the south (Shin et al., 2020; Hakim et al., 2022b). Based on the interferogram simulation, we can see the recorded deformations of 7, 14, and 28 cm in Figures 6A,B,C, respectively. This deformation is thought to be caused by the presence of lava pads around the

Cheorwon area, which is now flat land that spreads widely around the Orisan Mountain. The level of deformation is based on the probability of volume changes that emerged by taking into account the geological aspects at that time; this can be achieved by simulating lava flows, as in previous research (Hakim et al., 2022b).

In addition, we attempted to use the combined error simulation and deformation simulation data to form a wrapped interferogram simulation. Simulations of topographic error, atmospheric disturbance, and orbital error were used in the process of generating the synthetic phase of the interferogram. The combination of the interferogram simulation data was used for the deep learning training process in identifying deformation patterns. The use of the wrapped interferogram phase has the advantage of identifying features for the machine learning training process because of the presence of fringes in the interferogram phase. To increase the capacity of the training data, the synthesis phase was carried out with data augmentation. With the increase in sample training data, the goal was to balance the machine learning process. There are several data augmentation options, including 1) horizontal and vertical flipping, 2) image rotation with angles of 15°, 30°, and 45° and 3) image distortion with pixel variations on the horizontal and vertical axes. The results of the augmented data for the interferogram images are shown in Figure 7. More than 1,000 images were used in the deep learning training process after augmented data were applied; as

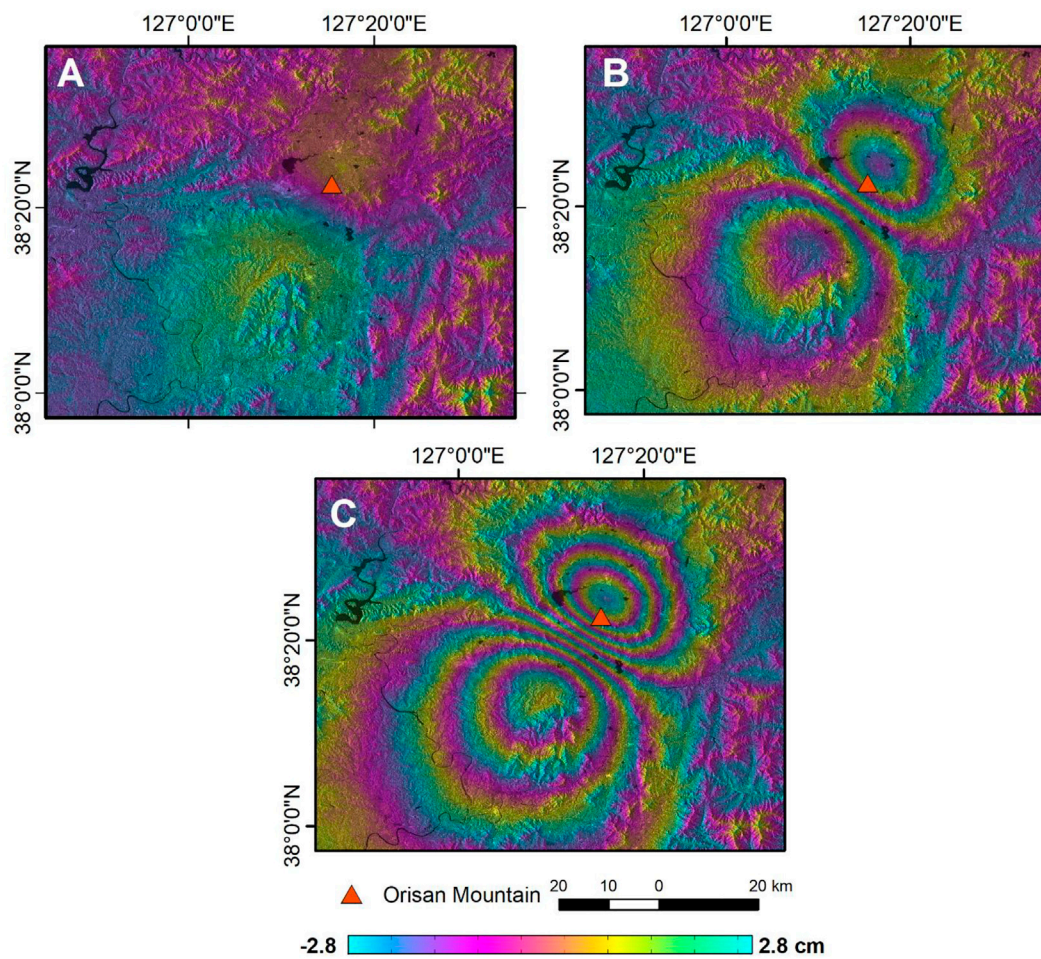


FIGURE 6
Synthetic interferogram results of the Orisan Mountain with different VEs: (A) Vei 1, (B) Vei 2, and (C) Vei 3.

a result, the algorithm learned shapes and extracted the useful information from the available dataset. In addition, the increase in the dataset can help to overcome the imbalanced data, which is commonly found in machine learning processes.

Deep learning performance analysis

In this research, we used a transfer learning approach with a pretrained network as opposed to training a new network. By using this training approach, there is an advantage in terms of time efficiency, where the pretrained network features are pretrained using a large number of images and various types of natural images. In general, the pretrained network can classify images into 1,000 categories, but we adjusted the network to achieve our identification goal. Therefore, we used two classification categories, namely, deformation and non-deformation, for the first dataset. Meanwhile, four

classification categories were used in the second dataset. Adjustments to the training layer, such as the fully connected layer, were also made to achieve classification into the chosen categories. The operating parameters used include a maximum epoch of 50 and a batch size of 100. The final probability was the output of each network structure for image classification.

In this research, three pretrained network architectures were used for deformation classification, namely, ResNet-18, ResNet-50, and AlexNet, which have been popular and used in previous research. The performance of the three architectures was objectively evaluated by using the receiver operating characteristic curve (ROC curve) (Fawcett, 2006). This curve is used to describe the identification performance by comparing the true positive rate and the false-positive rate. Quantitatively, machine learning performance is indicated by the area under the curve (AUC) result, which is the integrated area under the ROC curve. The higher the AUC values (maximum = 1), the better the performance, with an AUC = 0.8 indicating good performance

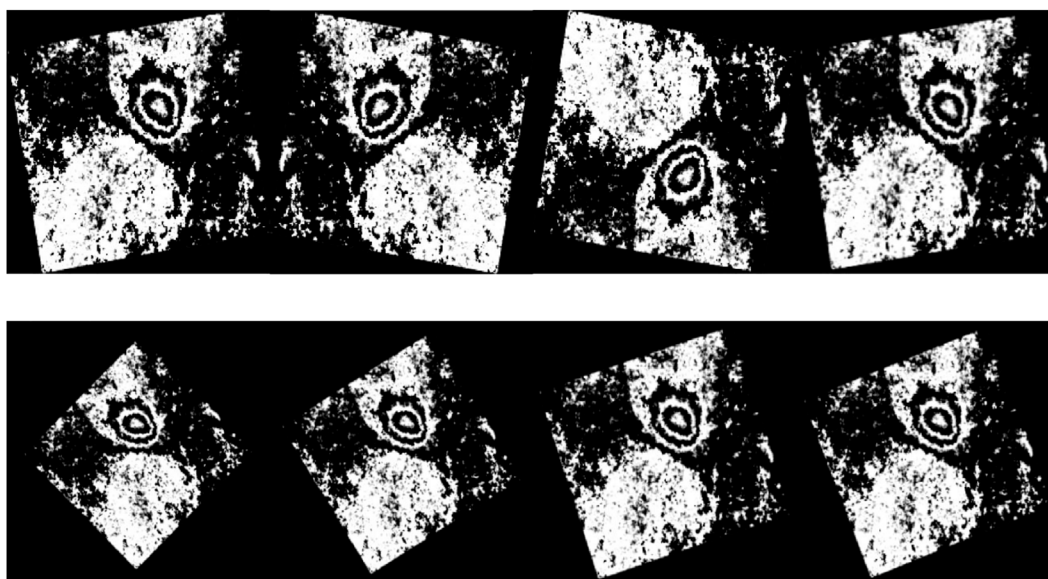


FIGURE 7

Data augmented image of a synthetic interferogram to training the CNN model to overcome imbalance and limited data in the training datasets.

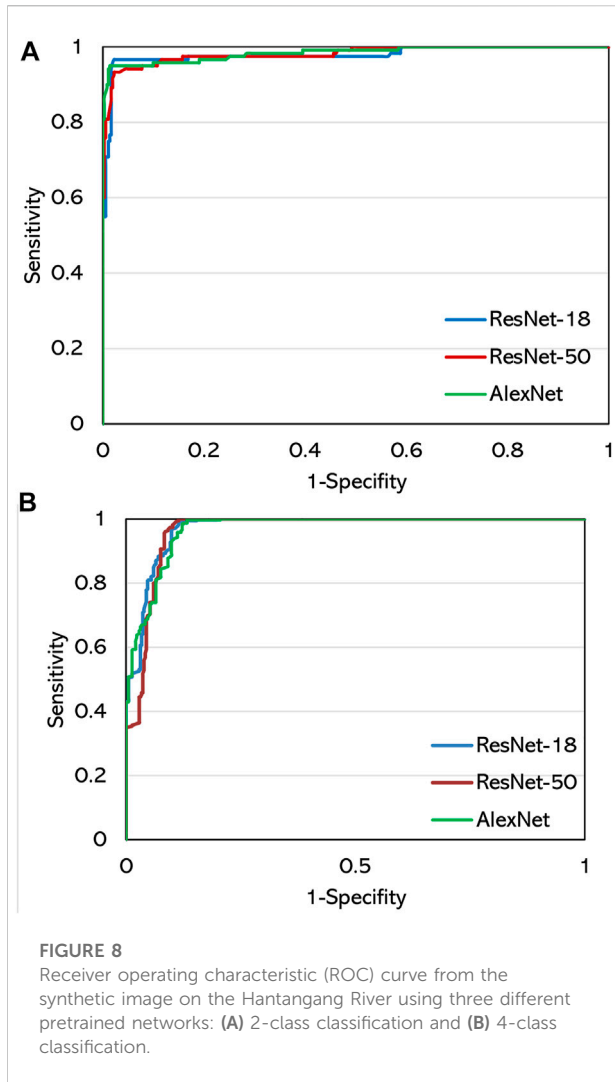
(Lee and Park, 2013). As a result, the AUC values of ResNet-18, ResNet-50, and AlexNet were 0.968, 0.965, and 0.955, respectively, for the 2-class label classification categories, as shown in Figure 8A. In Figure 8B, for the 4-class label classification categories, the AUC values were 0.978, 0.981, and 0.983 for ResNet-18, ResNet-50, and AlexNet, respectively.

Discussion

In this study, we have demonstrated the capability of the deep learning convolutional neural network (CNN) algorithm in classifying interferogram images based on synthetic data. This algorithm has also demonstrated its capability in processing images of interferograms as part of machine learning training on large datasets. The performance of the model is quantitatively evaluated based on the confusion matrix. The confusion matrix performs a quantitative analysis based on the true positive and true negative as the correct classification and false-positive and false negative in the incorrect classification (Truong et al., 2018). The combination of these assessments can be translated into the accuracy of model performance. In Table 1, a comparison of the performance accuracy values for each network structure with the type of training dataset is given. In the 2-class datasets, the highest accuracy of 94.01% was achieved using AlexNet. The accuracies of ResNet-18 and ResNet-50 followed with values of 92.58% and 93.62%, respectively. Meanwhile, in the 4-class datasets, the highest accuracy, which was above 90%, indicating good performance, was achieved using ResNet-18;

ResNet-18 performed 2% better than the other network structures. This decrease in accuracy is a result of the 1.93% increase in false-positives for the ResNet-50 structure, while there is a 2.63% increase in false negatives when using AlexNet compared to using ResNet-50.

In addition, the accuracy of detecting the deformation interferogram generated by CNN is high, as values of >85% were achieved using each network architecture. Further analysis can be carried out to identify features that are used as references for determining the classification of surface deformation in the input image data. One of the methods used to visualize and reason detection in CNN is the class activation map (CAM) (Bregman and Barnhart, 2021). CAM is the visualization of information deep in the network, specifically the weights of the last convolution layer (Feng et al., 2021). The CAM is an intensity map that highlights the region of pixels that correspond to a certain class activation value. This approach is useful for recognizing machine learning progress in the determination of the classification of input images into certain categories (Kwásniewska et al., 2017). As the result, we use two images of deformation images in Figures 9A,B and noise data in Figure 9C. For example, Figures 9D,E show the correlation of pattern recognition between the deformation images, while Figure 9F shows the correlation between the inputs of the classified noise data. The probability levels are 98% and 91.2% for the deformation in Figures 9D,E, respectively, and 90.4% for the disturbance in Figure 9F. This analysis provides an interesting picture of how a system can recognize input data after machine learning training has



taken place. The correlation results also show that the deep learning algorithm is quite reliable in detecting interferogram deformation.

As a result, CNN can be a breakthrough model in its application to detect the deformation phase of the wrapped InSAR data. In addition, the use of synthetic data in CNN

training provides an advantage compared to relying solely on real interferogram data. The process of augmenting data on the dataset also provides an advantage in time efficiency by providing learning input for CNN to obtain optimal results (Panahi et al., 2020). The use of these various approaches has resulted in the ability to overcome some limitations, such as the small number of observed deformation signals.

Therefore, the results from these approaches can be developed for rapid deformation detection based on SAR data in the future. In the case of this study, the detection of deformation is focused on the area of the ancient Orisan volcano which had eruptions more than before the last century which is still rarely the object of research. Volcanic activity on the Korean peninsula has attracted the attention of researchers to study the characteristics of volcanoes in the past. In previous research, the Orisan volcano has been modeled using a 3D printer to study lava flows in HVRF by simulating lava flows (Hakim et al., 2022b). In addition, the use of machine learning is also carried out in the process of classifying lava flows in computer and physical simulation processes. Even so, there are some limitations that faced in this research from the characteristic deformation and typical simulations of signal used in this research. In this research we try to employ the Okada model as source deformation to simulate the deformation in eruption event in Orisan mountain. The use of the deformation model is still limited to one type of deformation model, namely, the Okada model. By carrying out further tests for various deformation characteristics, it is possible to determine the reliability of this technique in detecting sources of deformation such as anthropogenic effects, including resource extraction or other forms of signal deformation patterns (Anantrasirichai et al., 2019). Consequently, this limitation leads to inflexibility in the detection of deformations with other characteristics. In addition, hardware limitations are one of the other current challenges in processing large amounts of data. Activation of the pooling layer and managerial data processing is some of the future improvisation efforts that will be made to obtain maximum results under more efficient conditions (Bregman and Barnhart, 2021). The characteristics of the

TABLE 1 Performance analysis of the CNN pretrained network in each class dataset.

Evaluation criteria	2-class datasets			4-class datasets		
	ResNet-18	ResNet-50	AlexNet	ResNet-18	ResNet-50	AlexNet
Overall accuracy	92.58	93.62	94.01	97.82	95.75	94.99
Error rate	7.42	6.38	5.99	2.17	4.25	5.01
True positive rate	3.39	98.27	96.94	95.64	94.46	93.98
False-positive rate	96.32	1.56	2.86	1.45	3.38	4.00
False negative rate	11.46	11.20	9.11	4.34	6.29	6.97

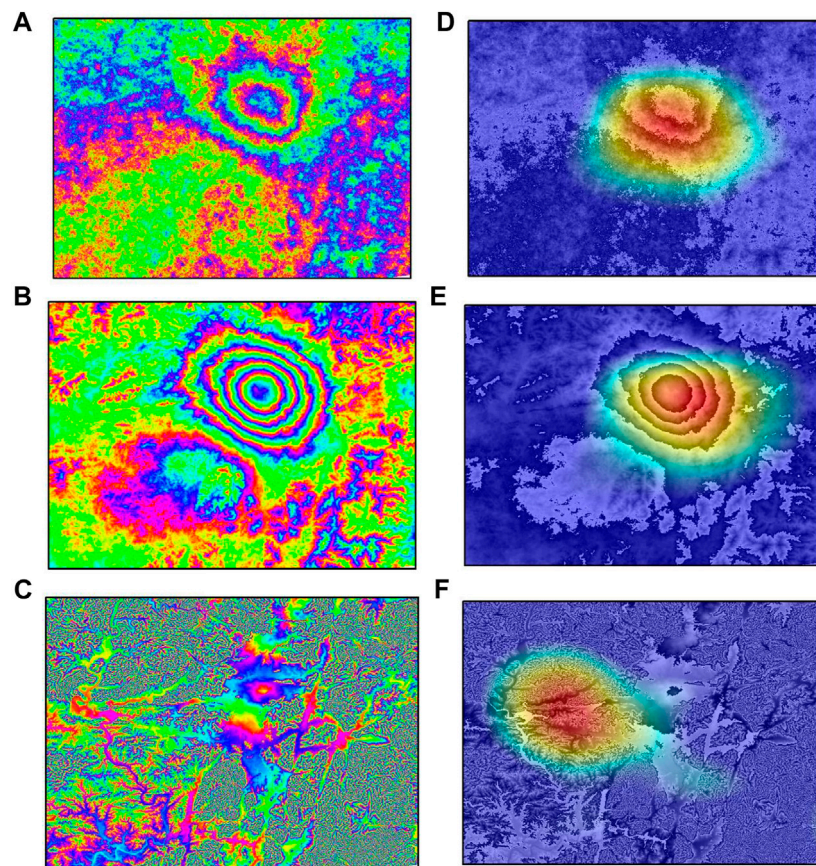


FIGURE 9

Input image from training dataset (A) synthesis deformation label, (B) synthesis deformation label, (C) atmospheric label and overlaid CAM analysis of image (D) deformation label with a probability of 98%, (E) deformation label with a probability of 91.2%, and (F) atmospheric label image with a probability 90.7%. The red area of the CAM represents a high probability of classification detection.

error simulation can also affect the performance of the detection with given the limitations of the error simplification made in this study. Such coherence characteristics in the study area, which influence the formation of the interferogram, were not considered at this time. Regions with a low level of coherence can provide random phase disturbances that are difficult to interpret. Other developments also need to be considered with the application of unwrapping phase data, which is useful in detecting continuous deformation.

In addition to the various limitations faced, there are still some potentials that arise. Based on previous research, the use of the Mogi model as a source of deformation still limits the influence of other sources of deformation, such as an earthquake that occurs during an eruption (MacQueen et al., 2020). Therefore, in this research the Okada method is used as a deformation model in the synthesis of interferograms which is expected to provide a better image in the training process on the deformation signal. Even so, in practice there are still some

vulnerabilities in identifying interferograms such as ionospheric problems or interference with the unwrap process that often arise (Rongier et al., 2019). The combination of these errors can be integrated in the development of deformation detection with machine learning in the future process. The InSAR approach that describes simulations is a potential in this study area research, especially in studying ancient volcanic eruptions. By looking at the potential for detecting the InSAR deformation pattern in this area, it is hoped that it can be applied to other areas, especially in the case of real eruptions for mitigation mapping efforts. The use of the algorithm this research has the potential for development in a wider direction, because of the limitations of the simulation signal on the interferogram, various other inputs are needed to complete the rapid detection progress. Spatial input data such as geological conditions, volcanic activity, and others-relative factor can be input in the mapping process or deformation detection. Therefore, the application of optimized algorithm can be integrated in this further research to overcome the

limitations in operational parameter to minimize the interference of trial and error (Tien Bui et al., 2017). Therefore, the usefulness of machine learning algorithm can be integrated to retrieve the time-series deformation in the future (Sun et al., 2020). However, the currently application of the rapid detection of SAR data based on deep learning is an initial approach to cases of past eruptions such as the Hantangang UNESCO Global Geopark. Further research can be continued to improve the existing limitations and can be applied to several other deformation characteristics as a rapid detection effort that is useful in risk management.

Conclusion

This research provides a knowledge-gaining framework that routinely searches through large amounts of wrapped InSAR data to rapidly detect deformation. The synthesis of this interferogram is based on a simulation of a volcanic eruption that previously occurred in Hantangang. With the limitation of deformation data, the use of synthetic data is a solution to understanding deformation detection. In addition to these limitations, the use of augmented data is one solution to avoid data imbalance and enrich the training dataset to achieve optimal results. In addition to the deformation synthesis, we also perform error simulations including atmospheric disturbances, topographical errors, and orbital errors. The combination of deformation and error synthesis is then used in the interferogram synthesis.

In terms of performance, a CNN deep learning model is used to carry out the learning process using datasets from interferogram synthesis. The pretrained network is used to streamline the performance of training the model and has shown its reliability on ResNet-18, ResNet-50, and AlexNet. Based on the performance analysis using AUC, it was found that the analytical model can detect deformation with an accuracy greater than 85%. In addition, based on the class activation map (CAM), which can visualize machine detection, high probability can be achieved. This shows the potential use of CNN in the rapid detection of interferogram data in the future. However, some limitations are still an obstacle in this research. The limited amount of previous deformation data provides an overview of the deformation when the event occurred. Then, the limitations of the deformation model are used to make it possible to be inflexible in recognizing other deformation characteristics. Therefore, development can be achieved by increasing the enrichment of more varied deformation characteristics so that various types of deformation can be detected. The enrichment of error simulation data is also useful for studying errors that arise in the case of interferogram deformation. In addition, the application of unwrapping interferogram data can also provide interesting research in the detection of slow and continuous deformation. Besides, the

development of machine learning algorithm can be carried in the future for using optimizing algorithm and integrated to retrieve time-series deformation measurement. In general, this study is an initial study reconstructing past deformations and projects in the rapid detection of deformation based on SAR data.

Data availability statement

The datasets presented in this study can be found in online repositories. The names of the repository/repositories and accession number(s) can be found below: <https://asf.alaska.edu/>.

Author contributions

MF, DK, and C-WL jointly developed the concept of this paper, and WH led the writing of this paper. MF processed the InSAR data and conducted the modeling of all datasets. WH and SP collected the InSAR data and assisted with the use of the modeling software. C-WL, Y-CP, C-HK, and DK supervised of writing this paper. SP, Y-CP, and C-HK conducted project administration. All authors contributed to the writing of the paper.

Funding

This research was supported by the 2021 Research Project for the UNESCO Hantangang River Global Geopark and the Gyeonggi Provincial Office and by the Basic Science Research Program through the National Research Foundation of Korea (NRF) funded by the Ministry of Education (No. 2019R1A6A1A03033167) also founded by the Korea Institute of Ocean Science and Technology (Grant Number. PEA0016).

Conflict of interest

The authors declare that the research was conducted in the absence of any commercial or financial relationships that could be construed as a potential conflict of interest.

Publisher's note

All claims expressed in this article are solely those of the authors and do not necessarily represent those of their affiliated organizations, or those of the publisher, the editors and the reviewers. Any product that may be evaluated in this article, or claim that may be made by its manufacturer, is not guaranteed or endorsed by the publisher.

References

- Achmad, A. R., Lee, S., Park, S., Eom, J., and Lee, C. W. (2020). Estimating the potential risk of the Mt. Baekdu Volcano using a synthetic interferogram and the LAHARZ inundation zone. *Geosci. J.* 24, 755–768. doi:10.1007/s12303-020-0032-9
- Albino, F., Biggs, J., and Syhbabana, D. K. (2019). Dyke intrusion between neighbouring arc volcanoes responsible for 2017 pre-eruptive seismic swarm at Agung. *Nat. Commun.* 10, 1–11. doi:10.1038/s41467-019-08564-9
- Amelung, F., Galloway, D. L., Bell, J. W., Zebker, H. A., and Lacznaiak, R. J. (1999). Sensing the ups and downs of las vegas: InSAR reveals structural control of land subsidence and aquifer-system deformation. *Geol.* 27, 483–486. doi:10.1130/0091-7613(1999)027<0483:stuado>2.3.co;2
- Anantrasirichai, N., Biggs, J., Albino, F., and Bull, D. (2019). A deep learning approach to detecting volcano deformation from satellite imagery using synthetic datasets. *Remote Sens. Environ.* 230, 111179. doi:10.1016/j.rse.2019.04.032
- Bagnardi, M., and Hooper, A. (2018). Inversion of surface deformation data for rapid estimates of source parameters and uncertainties: A bayesian approach. *Geochem. Geophys. Geosyst.* 19, 2194–2211. doi:10.1029/2018GC007585
- Biggs, J., and Pritchard, M. E. (2017). Global volcano monitoring: What does it mean when volcanoes deform? *Elements* 13, 17–22. doi:10.2113/gselements.13.1.17
- Biggs, J., Wright, T., Lu, Z., and Parsons, B. (2007). Multi-interferogram method for measuring interseismic deformation: Denali Fault, Alaska. *Geophys. J. Int.* 170, 1165–1179. doi:10.1111/j.1365-246X.2007.03415.x
- Biggs, J., Ebmeier, S. K., Aspinall, W. P., Lu, Z., Pritchard, M. E., Sparks, R. S. J., et al. (2014). Global link between deformation and volcanic eruption quantified by satellite imagery. *Nat. Commun.* 5, 1–7. doi:10.1038/ncomms4471
- Bonforte, A., Guglielmino, F., and Puglisi, G. (2019). Large dyke intrusion and small eruption: The December 24, 2018 Mt. Etna eruption imaged by Sentinel-1 data. *Terranova.* 31, 405–412. doi:10.1111/ter.12403
- Brengman, C. M. J., and Barnhart, W. D. (2021). Identification of surface deformation in InSAR using machine learning. *Geochem Geophys Geosyst.* 22, e2020GC009204. doi:10.1029/2020GC009204
- Caricchi, L., Townsend, M., Rivalta, E., and Namiki, A. (2021). The build-up and triggers of volcanic eruptions. *Nat. Rev. Earth Environ.* 2, 458–476. doi:10.1038/s43017-021-00174-8
- Casadevall, T. J., Tormey, D., and Roberts, J. (2019a). *World heritage volcanoes: Classification, gap analysis, and recommendations for future listings.* Gland, Switzerland. doi:10.2305/iucn.ch.2019.07.en
- Casadevall, T. J., Tormey, D., and Van Sisting, D. (2019b). Protecting our global volcanic estate: Review of international conservation efforts. *Int. J. Geoheritage Parks* 7, 182–191. doi:10.1016/j.ijgeop.2020.01.002
- Cho, I. H., Kim, H. K., Lee, M. H., Kim, Y. J., Lee, H., and Kim, B. H. (2020). *The effect of monsoon rainfall patterns on epilithic diatom communities in the hantangang river, Korea*, 12, 1471. doi:10.3390/w12051471 The effect of monsoon rainfall patterns on epilithic diatom communities in the Hantangang River, Korea *Water*
- Coleman, T. F., and Li, Y. (1994). On the convergence of interior-reflective Newton methods for nonlinear minimization subject to bounds. *Math. Program.* 67, 189–224. doi:10.1007/BF01582221
- De Novellis, V., Atzori, S., De Luca, C., Manzo, M., Valerio, E., Bonano, M., et al. (2019). DInSAR analysis and analytical modeling of Mount Etna displacements: The december 2018 volcano-tectonic crisis. *Geophys. Res. Lett.* 46, 5817–5827. doi:10.1029/2019GL082467
- Doblas, J., Shimabukuro, Y., Sant'Anna, S., Carneiro, A., Aragão, L., and Almeida, C. (2020). Optimizing near real-time detection of deforestation on tropical rainforests using sentinel-1 data. *Remote Sens.* 12, 3922. doi:10.3390/RS12233922
- Fadhillah, M. F., and Lee, C. W. (2021). The estimated source of 2017 Pohang earthquake using surface deformation modeling based on multi-frequency InSAR data. *Korean J. Remote Sens.* 37, 57–67. doi:10.7780/kjrs.2021.37.1.5
- Farr, T. G., Rosen, P. A., Caro, E., Crippen, R., Duren, R., Hensley, S., et al. (2007). The shuttle radar topography mission. *Rev. Geophys.* 45, 183. doi:10.1029/2005RG000183
- Faul, H. (1960). Geologic time scale. *Geol. Soc. Am. Bull.* 71, 637–644. doi:10.1130/0016-7606(1960)71[637:gts]2.0.co;2
- Fawcett, T. (2006). An introduction to ROC analysis. *Pattern Recognit. Lett.* 27, 861–874. doi:10.1016/j.patrec.2005.10.010
- Feng, Z., Ji, H., Stanković, L., Fan, J., and Zhu, M. (2021). SC-SM CAM: An efficient visual interpretation of CNN for SAR images target recognition. *Remote Sens.* 13, 4139. doi:10.3390/RS13204139
- Garg, R., Kumar, A., Bansal, N., Prateek, M., and Kumar, S. (2021). Semantic segmentation of PolSAR image data using advanced deep learning model. *Sci. Rep.* 11, 1–18. doi:10.1038/s41598-021-94422-y
- Ghosh, B., Motagh, M., Haghighi, M. H., Vassileva, M. S., Walter, T. R., and Maghsudi, S. (2021). Automatic detection of volcanic unrest using blind source separation with a minimum spanning tree based stability analysis. *IEEE J. Sel. Top. Appl. Earth Obs. Remote Sens.* 14, 7771–7787. doi:10.1109/JSTARS.2021.3097895
- Hakim, W. L., Nur, A. S., Rezaie, F., Panahi, M., Lee, C. W., and Lee, S. (2022a). Convolutional neural network and long short-term memory algorithms for groundwater potential mapping in Anseong, South Korea. *J. Hydrology Regional Stud.* 39, 100990. doi:10.1016/j.ejrh.2022.100990
- Hakim, W. L., Ramayanti, S., Park, S., Ko, B., Cheong, D.-K., and Lee, C.-W. (2022b). Estimating the pre-historical volcanic eruption in the Hantangang River volcanic field: Experimental and simulation study. *Remote Sens.* 14, 894. doi:10.3390/RS14040894
- Hakim, W. L., Rezaie, F., Nur, A. S., Panahi, M., Khosravi, K., Lee, C.-W., et al. (2022c). Convolutional neural network (CNN) with metaheuristic optimization algorithms for landslide susceptibility mapping in Icheon, South Korea. *J. Environ. Manag.* 305, 114367. doi:10.1016/j.jenvman.2021.114367
- He, K., Zhang, X., Ren, S., and Sun, J. (2016). “Deep residual learning for image recognition,” in Proceeding of the 2016 IEEE Conference on Computer Vision and Pattern Recognition, Las Vegas, NV, USA, December 2016 (IEEE), 770–778. doi:10.1109/CVPR.2016.90
- Iio, K., and Furuya, M. (2018). Surface deformation and source modeling of Ayaz-Akhtarma mud volcano, Azerbaijan, as detected by ALOS/ALOS-2 InSAR. *Prog. Earth Planet. Sci.* 5, 1–16. doi:10.1186/S40645-018-0220-7/FIGURES/14
- Keszthelyi, L., and Self, S. (1998). Some physical requirements for the emplacement of long basaltic lava flows. *J. Geophys. Res.* 103, 27447–27464. doi:10.1029/98jb00606
- Kil, Y., Ahn, K. S., Woo, K. S., Lee, K. C., Jwa, Y. J., Jung, W., et al. (2019). Geoheritage values of the quaternary Hantangang River volcanic field in the central Korean peninsula. *Geoheritage* 11, 765–782. doi:10.1007/s12371-018-0329-5
- Krizhevsky, A., Sutskever, I., and Hinton, G. E. (2017). ImageNet classification with deep convolutional neural networks. *Commun. ACM* 60, 84–90. doi:10.1145/3065386
- Kwasniewska, A., Ruminski, J., and Rad, P. (2017). “Deep features class activation map for thermal face detection and tracking,” in Proceeding of the 2017 10th International Conference on Human System Interactions (HSI), Ulsan, Korea (South), July 2017 (IEEE), 41–47. doi:10.1109/HSI.2017.8004993
- Lapini, A., Pettinato, S., Santi, E., Paloscia, S., Fontaneli, G., and Garzelli, A. (2020). Comparison of machine learning methods applied to SAR images for forest classification in mediterranean areas. *Remote Sens.* 12, 369. doi:10.3390/RS12030369
- Lee, C. W., Lu, Z., and Jung, H. S. (2012). Simulation of time-series surface deformation to validate a multi-interferogram InSAR processing technique. *Int. J. Remote Sens.* 33, 7075–7087. doi:10.1080/01431161.2012.700137
- Lee, H., and Oh, J. (2018). Establishing an ANN-based risk model for ground subsidence along railways. *Appl. Sci.* 8, 1936. doi:10.3390/app8101936
- Lee, J., and Shin, D. (2019). Analysis of educational signboards in the national geoparks for the educational use. *jgsk* 55, 703–726. doi:10.14770/jgsk.2019.55.6.703
- Lee, S., and Kim, T. (2021). Parallel dislocation model implementation for earthquake source parameter estimation on multi-threaded GPU. *Appl. Sci.* 11, 9434. doi:10.3390/APP11209434
- Lee, S., and Park, I. (2013). Application of decision tree model for the ground subsidence hazard mapping near abandoned underground coal mines. *J. Environ. Manag.* 127, 166–176. doi:10.1016/j.jenvman.2013.04.010
- Li, J., Xu, C., Su, H., Gao, L., and Wang, T. (2022). Deep learning for SAR ship detection: Past, present and future. *Remote Sens.* 14, 2712. doi:10.3390/RS14112712
- Li, Z., and Bethel, J. (2008). Image coregistration in SAR interferometry. *Proc. Int. Arch. Photogramm. Remote Sens. Spat. Inf. Sci.* XXXVII, 433–438.
- Long, J., Shelhamer, E., and Darrell, T. (2015). “Fully convolutional networks for semantic segmentation,” in Proceeding of the 2015 IEEE Conference on Computer Vision and Pattern Recognition (CVPR), Boston, MA, USA, June 2015 (IEEE), 3431–3440. doi:10.1109/CVPR.2015.7298965
- MacQueen, P., Delgado, F., Reath, K., Pritchard, M. E., Bagnardi, M., Milillo, P., et al. (2020). Volcano-tectonic interactions at sabancaya volcano, Peru: Eruptions, magmatic inflation, moderate earthquakes, and fault creep. *JGR Solid Earth* 125, e2019JB019281. doi:10.1029/2019JB019281

- Marghany, M. (2012a). DInSAR technique for three-dimensional coastal spit simulation from radarsat-1 fine mode data. *Acta Geophys.* 61, 478–493. doi:10.2478/S11600-012-0061-5
- Marghany, M. (2012b). Three-dimensional coastal geomorphology deformation modelling using differential synthetic aperture interferometry. *Z. für Naturforsch. - Sect. A J. Phys. Sci.* 67, 419–420. doi:10.5560/ZNA.2012-0031/MACHINEREADABLECITATION/RIS
- Masterlark, T. (2007). Magma intrusion and deformation predictions: Sensitivities to the Mogi assumptions. *J. Geophys. Res.* 112, 4860. doi:10.1029/2006JB004860
- Milillo, P., Sacco, G., Di Martire, D., and Hua, H. (2022). Neural network pattern recognition experiments toward a fully automatic detection of anomalies in InSAR time series of surface deformation. *Front. Earth Sci.* 9, 1132. doi:10.3389/FEART.2021.728643/BIBTEX
- Mogi, K. (1958). Relations between the eruption of various volcanoes and the deformation of the ground surfaces around them. *Bulletion Earthq. Res. Inst.* 36, 99–134.
- Moré, J. J. (1978). "The Levenberg-Marquardt algorithm: Implementation and theory," in *Numerical analysis*, 105–116. doi:10.1007/BFB0067700
- Németh, K., Casadevall, T., Moufti, M. R., and Marti, J. (2017). Volcanic geoheritage. *Geoheritage* 9, 251–254. doi:10.1007/s12371-017-0257-9
- Newhall, C. G., and Self, S. (1982). The volcanic explosivity index (VEI) an estimate of explosive magnitude for historical volcanism. *J. Geophys. Res.* 87, 1231–1238. doi:10.1029/jc087ic02p01231
- Okada, Y. (1985). Surface deformation due to shear and tensile faults in a half-space. *Bull. Seismol. Soc. Am.* 75, 1135–1154. doi:10.1785/BSSA0750041135
- Okada, Y., and Yamamoto, E. (1991). Dyke intrusion model for the 1989 seismovolcanic activity off Ito, central Japan. *J. Geophys. Res.* 96, 10361. doi:10.1029/91jb00427
- Panahi, M., Gayen, A., Pourghasemi, H. R., Rezaie, F., and Lee, S. (2020). Spatial prediction of landslide susceptibility using hybrid support vector regression (SVR) and the adaptive neuro-fuzzy inference system (ANFIS) with various metaheuristic algorithms. *Sci. Total Environ.* 741, 139937. doi:10.1016/j.scitotenv.2020.139937
- Remy, D., Froger, J. L., Perfettini, H., Bonvalot, S., Gabalda, G., Albino, F., et al. (2014). Persistent uplift of the Lazufre volcanic complex (Central Andes): New insights from PCAIM inversion of InSAR time series and GPS data. *Geochem. Geophys. Geosyst.* 15, 3591–3611. doi:10.1002/2014GC005370
- Remy, D., Chen, Y., Froger, J. L., Bonvalot, S., Cordoba, L., and Fustos, J. (2015). Revised interpretation of recent InSAR signals observed at Llainma volcano (Chile). *Geophys. Res. Lett.* 42, 3870–3879. doi:10.1002/2015GL063872
- Ripepe, M., Donne, D. D., Genco, R., Maggio, G., Pistolesi, M., Marchetti, E., et al. (2015). Volcano seismicity and ground deformation unveil the gravity-driven magma discharge dynamics of a volcanic eruption. *Nat. Commun.* 6, 7998. doi:10.1038/ncomms7998
- Rongier, G., Rude, C., Herring, T., and Pankratius, V. (2019). Generative modeling of InSAR interferograms. *Earth Space Sci.* 6, 2671–2683. doi:10.1029/2018EA000533
- Ryu, S., Oka, M., Yagi, K., Sakuyama, T., and Itaya, T. (2011). K-Ar ages of the Quaternary basalts in the Jeongok area, the central part of Korean Peninsula. *Geosci. J.* 15, 1–8. doi:10.1007/s12303-011-0008-x
- Sameen, M. I., Pradhan, B., and Lee, S. (2020). Application of convolutional neural networks featuring Bayesian optimization for landslide susceptibility assessment. *Catena* 186, 104249. doi:10.1016/j.catena.2019.104249
- Seropian, G., Kennedy, B. M., Walter, T. R., Ichihara, M., and Jolly, A. D. (2021). A review framework of how earthquakes trigger volcanic eruptions. *Nat. Commun.* 12, 1–13. doi:10.1038/s41467-021-21166-8
- Shin, S., Cheon, Y., Choi, J. H., Cheong, D., Choi, S. Y., Lim, H. S., et al. (2020). Late Pleistocene sedimentary environment and reverse faulting along the chugaryung fault in the central Korean peninsula: A case study on the Cheorwon basin. *Geosci. J.* 24, 615–623. doi:10.1007/s12303-020-0026-7
- Siebert, L., Cottrell, E., Venzke, E., and Andrews, B. (2015). "Earth's volcanoes and their eruptions: An overview," in *The encyclopedia of volcanoes* (Elsevier), 239–255. doi:10.1016/B978-0-12-385938-9.00012-2
- Song, S. G., and Lee, H. (2019). Static slip model of the 2017 Mw 5.4 pohang, South Korea, earthquake constrained by the InSAR data. *Seismol. Res. Lett.* 90, 140–148. doi:10.1785/0220180156
- Sreejith, K. M., Agrawal, R., Agram, P., and Rajawat, A. S. (2020). Surface deformation of the Barren Island volcano, Andaman Sea (2007–2017) constrained by InSAR measurements: Evidence for shallow magma reservoir and lava field subsidence. *J. Volcanol. Geotherm. Res.* 407, 107107. doi:10.1016/j.jvolgeores.2020.107107
- Sun, J., Wauthier, C., Stephens, K., Gervais, M., Cervone, G., La Femina, P., et al. (2020). Automatic detection of volcanic surface deformation using deep learning. *J. Geophys. Res. Solid Earth* 125, 19840. doi:10.1029/2020JB019840
- Tien Bui, D., Bui, Q. T., Nguyen, Q. P., Pradhan, B., Nampak, H., and Trinh, P. T. (2017). A hybrid artificial intelligence approach using GIS-based neural-fuzzy inference system and particle swarm optimization for forest fire susceptibility modeling at a tropical area. *Agric. For. Meteorology* 233, 32–44. doi:10.1016/j.agrformet.2016.11.002
- Truong, X., Mitamura, M., Kono, Y., Raghavan, V., Yonezawa, G., Truong, X., et al. (2018). Enhancing prediction performance of landslide susceptibility model using hybrid machine learning approach of bagging ensemble and logistic model tree. *Appl. Sci.* 8, 1046. doi:10.3390/app8071046
- Valade, S., Ley, A., Massimetti, F., D'Hondt, O., Laiolo, M., Coppola, D., et al. (2019). Towards global volcano monitoring using multisensor Sentinel missions and artificial intelligence: The MOUNTS monitoring system. *Remote Sens.* 11, 1528. doi:10.3390/rs11131528
- Valentine, G. A., and Connor, C. B. (2015). *Basaltic volcanic fields*. Second Edi. Elsevier, 423–439. doi:10.1016/b978-0-12-385938-9.00023-7
- Woo, K. S., Sohn, Y. K., Kil, Y., Jwa, Y. J., and Ju, S. O. (2018). "The aspiring Hantangang global geopark in Korea : Justification to be endorsed by UNESCO global geopark," in *EGU general assembly* (Vienna, Austria: EGU), 2935.
- Yang, Z., Li, Z., Zhu, J., Wang, Y., and Wu, L. (2020). Use of SAR/InSAR in mining deformation monitoring, parameter inversion, and forward predictions: A review. *IEEE Geosci. Remote Sens. Mag.* 8, 71–90. doi:10.1109/MGRS.2019.2954824
- Zhao, X., Wang, C., Zhang, H., Tang, Y., Zhang, B., and Li, L. (2021). Inversion of seismic source parameters from satellite InSAR data based on deep learning. *Tectonophysics* 821, 229140. doi:10.1016/J.TECTO.2021.229140